Velocity and density measurements in forced fountains with negative buoyancy

Fabio Addona,[1, a)] Luca Chiapponi,[2, b)] and Renata Archetti[1,c)]

[1)] *Department of Civil, Chemical, Environmental and Materials Engineering, Viale del Risorgimento 2, Università di Bologna, 40136 Bologna, Italy*

[2)] *Department of Engineering and Architecture (DIA), Parco Area delle Scienze, 181/A, Università degli Studi di Parma, 43124 Parma, Italy*

(Dated: 1 April 2021)

In fluid mechanics, fountains take place when a source fluid is driven by its own momentum into a surrounding ambient fluid and it is counterbalanced by buoyancy. These phenomena are largely encountered in nature and human activities. Despite the numerous studies on the subject, few experimental data are available about the internal structure of turbulent fountains. Here, we present a set of laboratory experiments with the aim to (i) get direct velocity and density measurements of fountains in a controlled environment and (ii) obtain insights about the basic physics of the phenomenon. The results concern the characteristics of the mean and turbulent flow: we report the analysis of the turbulent kinetic energy, the velocity skewness and the Reynolds stresses, including a quadrant analysis of the fluctuating velocities. For some tests, the correlation between density and vertical velocity is investigated for both mean and fluctuating values. We have quantified the momentum transport, which is mainly out-downward at the nozzle axis with peaks at the mean rise height, where also maximum levels of the buoyancy and mass fluxes are present. The ability of acoustic Doppler current profilers to identify the rise height of the fountain and to measure the velocity field is also discussed.

[a)] Electronic mail: fabio.addona@unibo.it

[b)] Electronic mail: luca.chiapponi@unipr.it

[c)] Electronic mail: renata.archetti@unibo.it

I. INTRODUCTION

Turbulent fountains are generally defined as localized vertical flows of a source fluid into an ambient fluid with different density. The result is a jet with opposing buoyancy invested by a return flow[1].

The research activity on fountains is justified by their widespread occurrence and range of practical applications. One of the main examples is the role of fountains in heating and cooling within buildings (e.g., in air conditioning)[2,3]. Fountains form as cool air is mechanically injected upward through floor-level cooling diffuser[4], and as warm air is injected downward to form curtains which are commonly used in tunnels and shop entrances as a means of segregating regions of fluid[5]. Fountains in the built environment also include those that may form more naturally (e.g., during an enclosure fire).

The interest in fountains is also strong in the geophysical sciences and environmental engineering. When a cloud tower is growing upwards into a dry environment, the evaporation of liquid water near the edge causes cooling, and hence a buoyancy inversion; the result is the formation of heavier fluid which drives the flow down again[6]. Other examples of natural fountains are the evolution of volcanic eruption columns[7], and the replenishment of magma chambers in the earth's crust (through the cyclic intrusion of pulses of dense magma that give rise to fountain-like flows)[8,9]. Hunt & Burridge[1] present a detailed review of many other applications that have been studied in the literature.

Different classes of fountains exist, and they can be defined depending on the source Froude number, $Fr_0 = w_0/\sqrt{g_0' r_0}$, where w_0 is the velocity at which fluid is ejected from the source, r_0 is the radial scale for the source, and g_0' is the buoyancy of the source fluid defined as $g_0' = g\left(\rho_0 - \rho_a\right)/\rho_a$, where ρ_0 and ρ_a are the densities of the source and ambient fluid, respectively. A typical classification is the one proposed by Kaye & Hunt[10], extended by Burridge & Hunt[11] and reported in Table I.

$0.3 \lesssim Fr_0 \lesssim 1.0$	very weak fountains
$1.0 \lesssim Fr_0 \lesssim 2.0$	weak fountains
$2.0 \lesssim Fr_0 \lesssim 4.0$	intermediate fountains
$Fr_0 \gtrsim 4.0$	forced and highly forced fountains

TABLE I. Classification of fountains according to the source Froude number.

Furthermore, fountains may be regarded as laminar for source Reynolds numbers $Re_0 \lesssim 120$, turbulent for $Re_0 \gtrsim 2000$, and transitional for $120 \lesssim Re_0 \lesssim 2000$, where $Re_0 = w_0 r_0/\nu$ with the representative kinematic viscosity, ν, typically taken as that of the source fluid. In addition, Burridge, Mistry, and Hunt[12] found that the threshold Reynolds number, Re_T, separating transitional to turbulent regime, is not constant and depends on the Froude number (with lower Re_T at lower Fr_0), and they proposed $Re_T = 75\,Fr_0 + 350$ for $Fr_0 > 2$.

The present works focuses on forced fountains. The dynamics of such fountains is characterized by a first pulse of fluid, that is a starting plume with a vortex-like front and nearly steady plume behind[6]. Afterwards the plume broadens, comes to rest and fell back. In fact, the fluid initially rises before the opposing buoyancy force arrests the flow and subsequently induces a returning counterflow (rise and fall behaviour). Finally, the fountain settles down to a nearly steady state, with an up-flow in the centre and a down-flow surrounding this. It is worth mentioning that the maximum distance from the source is reached by the first pulse. Figure 1 shows a schematic illustration of a forced fountain at the initial stage and during the subsequent steady state.

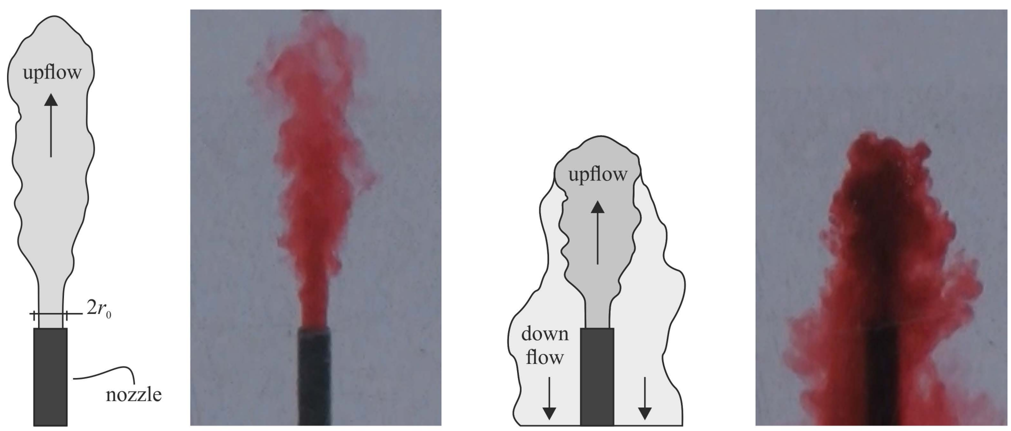

(a) (b) (c) (d)

FIG. 1. Scheme of a forced turbulent fountain: (a,b) at the initial stage and (c,d) during the subsequent steady state.

The approach to the subject is mainly experimental, with most of the literature studies regarding the steady, vertical, upwards injection of a heavy salt solution into a freshwater tank[2,6]. Several variants have been proposed, including the use of aqueous potassium chloride (KCl) solutions[13] and glycerol-water mixtures[14]; also downward ejections of positively buoyant source fluid have been generated, with jets of heated water into cooler water[15] or warm air into cool air[16]. A first theoretical approach was proposed by the pioneering work of Morton, Taylor, and Turner[17], and self-similar solutions have been further developed since then[18–20]. Self-similarity is widely encountered in the study of buoyancy- and gravity-driven phenomena, including gravity currents and Non-Newtonian flows[21].

Most of the experimental data available in the literature are represented by measurements of the bulk flow, mainly obtained with image processing techniques[1]. In the case of vertical turbulent jet with negative buoyancy, velocity profile measurements were obtained using hot film anemometer[15], while the flow structures were visualized by means of a Particle Image Velocimetry (PIV) system for transient positive and negative buoyant fountains[13]. More recently, PIV and planar laser induced fluorescence (PLIF) have been used to simultaneously measure the velocity and scalar concentration fields[22] and to give a first description of the turbulent structure[23]. However, additional experimental datasets and interpretations are needed to understand (i) the complex interaction between the upflow and the counterflow, and (ii) the phenomena related to the momentum and mass exchanges.

In this work we present experiments of forced fountains generated by the injection of dyed saltwater in homogeneous fresh water. Vertical and horizontal velocity profiles are acquired using an Acoustic Doppler Current Profiler (ADCP), and for some test also the vertical density profile is measured by means of a conductivity sensor. The aim of the paper is (i) to give further details about the mean flow and turbulence in fountains with negative buoyancy and (ii) to discuss the performance of the adopted instruments and techniques.

The paper is structured as follows. In §II, the experiments are described: facility and instrumentation are illustrated along with the data processing and methodology. Experimental results and their discussion are reported in §III, including the analysis of the turbulent kinetic energy, the velocity skewness, the Reynolds stresses, and a quadrant analysis of the fluctuating velocities. Main conclusions are summarized in §IV.

II. STUDY CASE AND METHODOLOGY

The present section describes the experimental setup and the experimental program. In addition, processing techniques and physical quantities are introduced, and some representative parameters of the tests are compared with the literature data for a better overview of the study case.

A. Experimental facility and programme

A series of experiments have been performed at the Hydraulics Laboratory of the University of Parma (Italy). As stated above, the experimental activity aimed to reproduce a vertical plume of a denser fluid which propagates into lighter fluid, thus subjected to a negative buoyancy. In these tests, we used dyed brine for the denser fluid forming the plume, and homogeneous fresh water for the ambient fluid.

The experimental apparatus consists of a square-section tank with dimensions $440 \times 440 \times 800\ \mathrm{mm}^3$, as shown in Figure 2. A vertical rigid tube with internal diameter $D_{int} = 7.8$ mm is fixed at the bottom of the tank and it protrudes upwards for a length of 300 mm. The tube is connected to an external pump, which allows the generation of fountains by injecting the salt water in the freshwater tank. A proportional–integral–derivative controller (PID) was used to control the flow rate, which was measured with a turbine flow-meter. The tank was filled with fresh water up to $600 - 650$ mm before starting the experiments.

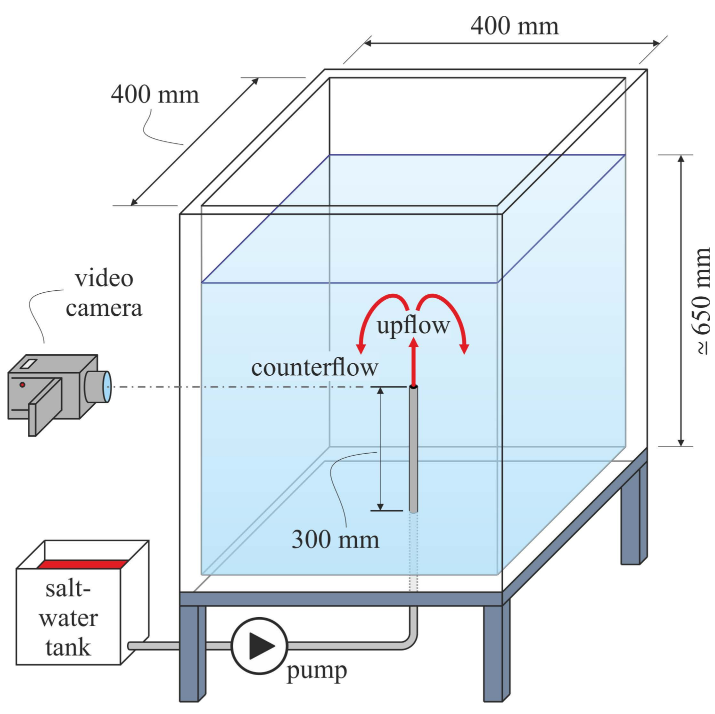

FIG. 2. Illustration of the experimental apparatus including the tank with fresh water, the rigid tube from which the dyed saltwater is injected, and the camera recording the experiment.

In a first set of experiments, a video camera with a resolution of 2 MP (1920 x 1080 pixels) was used to detect the interface between the ambient fluid (fresh-water) and the vertical plume (dyed salt-water), and hence to determine the main statistics of the fountain rise height. Before testing, a grid with known coordinates was inserted inside the tank and recorded for the extrinsic calibration of the camera, in order to transform the coordinate system from pixels to meters. During the test, the grid was removed to avoid disturbances to the flow.

A variable number of acoustic Doppler current profiler (DOP2000 by Signal Processing S.A.), hereinafter referred to as ADCP, have been placed inside the tank to measure velocity in the vertical (z) and horizontal (x) directions. The ADCP averages data within control volumes (gates) at incremental distances from the probe, providing instantaneous velocity profiles with a rate ≈ 20 Hz. Notice that such a sampling frequency makes it possible to observe turbulent structures at a scale that is not affected by the viscosity, and therefore that is substantially independent of the Reynolds number. The instrument we used is monostatic (i.e., it acts like a transceiver), and it is controlled by a computer which allows user to define a range of settings. We set an acoustic wave carrier with frequency of 8 MHz, a velocity measurements range of $\pm 320 \mathrm{mm\,s^{-1}}$ and a spatial resolution of 1.5 mm, which determined the spatial range $0-100$ mm starting from the probe. The estimated beam divergence angle is $\approx 2^{\circ}$, and the probe diameter is equal to 8 mm.

In order to filter the measurements, we disregarded velocity values with a number of echoes $N < N_t$, where the threshold value was taken as $N_t = \overline{N}_e/3$ and $\overline{N}_e$ is the time-averaged number of echoes (such a filtering is carried out independently for each value of z). In this way, we removed data with a poor backscatter which could increase the experimental uncertainty. Notice that (i) the injected fluid was seeded with TiO_2 particles, characterized by high sonic impedance, and (ii) a poor backscatter is associated to low (or null) tracer concentration in the ambient fluid. We calculated the Stokes number of the particles, Stk, which is an indicator of the fidelity of the flow tracers in turbulent flows, lower than 0.1, so the expected error due to the tracer is less than 1%[24]. For this reason no specific correction was applied to the velocity data. Vice versa, because the speed of sound depends on the density and temperature of the fluid, and to avoid errors of the order of 5%, we have corrected the position of the gate and the particle velocity using a model for density–bulk modulus–salinity suggested by Mackenzie[25].

A conductivity probe (Conduino) was installed together with the ADCP during some experiments. The primary sensor is represented by two pins (micro USB type B connectors) that work as electrodes spaced ≈ 0.2 mm. The volume of measurement is a cylinder of approximate height 4 mm and radius 2 mm, and the data rate is ≈ 20 Hz. The voltage output is proportional to the fluid salinity which, in turn, gives the instant value of the density in a point. Further details on this type of instrumentation and its applications can be found in Petrolo and Longo[26].

The configurations of the different experimental conditions are shown in Figure 3. For a first set of experiments (expts. 1-5, Figure 3a), the video camera was active and a single ADCP was installed at a fixed position measuring the vertical velocity profile above the inflow section. Then, for two experiments (expts. 6-7, Figure 3b) an ADCP was mounted together with the Conduino on a traverse system which continuously moved up and down in the tank during the experiments. This moving support covered the entire extension of the fountain with a velocity $\approx 6\,\mathrm{mm\,s^{-1}}$, allowing to obtain the profile of both vertical velocity and density. The Conduino was vertical, aligned with the source of the fountain, while the ADCP was mounted by the side with an inclination of 20 degrees. Finally, three ADCP were installed on the moving support (Figure 3c), two of which measuring vertical velocities (ADCP1 above the inflow section and ADCP2 with a horizontal offset of 10 mm) and one measuring horizontal velocity (ADCP3). In particular, expts. 8-10 were realized using ADCP1 and ADCP3 in movement; expts. 11-14 still involved ADCP1 and ADCP3 but in a fixed position; and expts. 15-20 were performed using all three probes in movement.

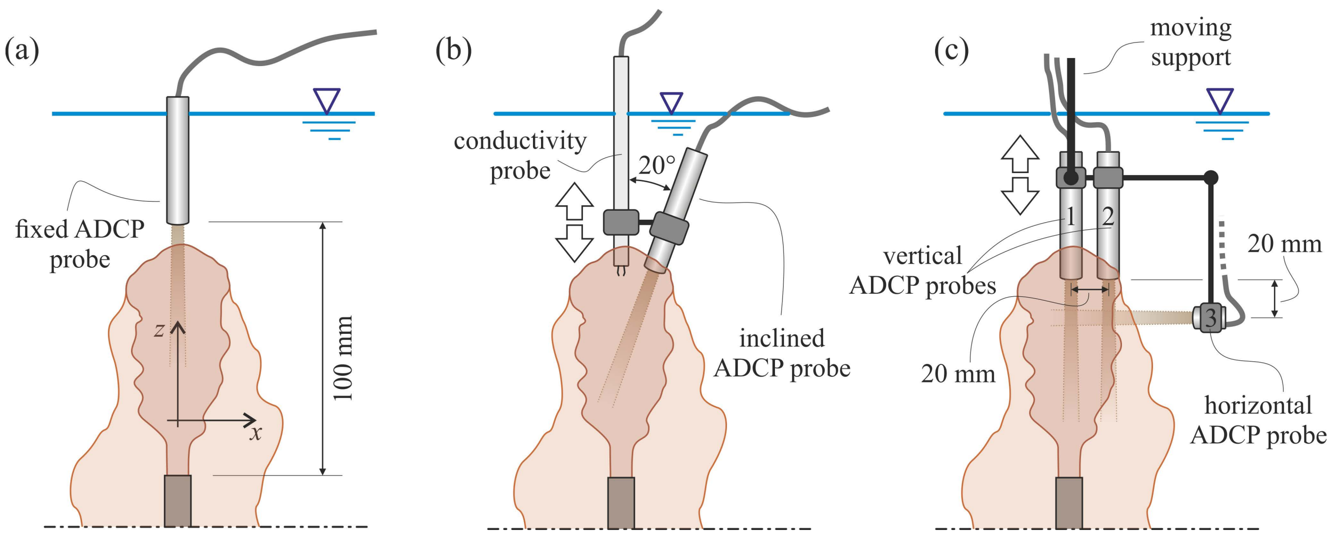

FIG. 3. Scheme of the probes configurations: (a) single ADCP at a fixed position; (b) vertical conductivity sensor (Conduino) and inclined ADCP; (c) vertical axial and non-axial probes (ADCP1 and ADCP2, respectively), together with the horizontal probe (ADCP3).

A linear potentiometer was connected to the traverse system and used to measure the position in time of the probes. An external trigger was used to start the experiments and the data acquisition (video, ADCP and Conduino).

The main parameters of the experiments are listed in Table II. In our experiments, the internal radius was $r_0 = D_{int}/2 = 3.8$ mm, the source fluid density was in the range $1020 \leq \rho_0 \leq 1092\,\mathrm{kg\,m^{-3}}$, and a value of source discharge $Q = 15\,\mathrm{ml\,s^{-1}}$ was used, which yields the source velocity $w_0 = Q/\left(\pi r_0^2\right) = 314\,\mathrm{mm\,s^{-1}}$. The ranges of the non-dimensional groups are $5.4 \pm 0.4 \leq Fr_0 \leq 16.4 \pm 1.4$ and $1030 \pm 70 \leq Re_0 \leq 1180 \pm 80$ at the inflow section, which indicate that we are dealing with (highly) forced fountains, following the classification by Burridge and Hunt[11] and Burridge and Hunt[27], herein BH2012 and BH2013, respectively. By adopting the relation proposed by Burridge, Mistry, and Hunt[12] (reported in §I), we find that all the fountains generated by the present activity can be considered turbulent, except for two tests (expts. 7 and 20) which are very close to the threshold and, in any case, far from the laminar conditions.

B. Physical quantities and scales

The main quantities that characterize the rise height and the rhythm of the fountains are the quasi-steady rise height z_{ss}, the fountain width $2\widetilde{b}_{ss}$, the mean rise height peak $\overline{z_{pe}}$ and the mean rise height trough $\overline{z_{tr}}$. The analytical values of the defined quantities are as follows:

$$z_{ss} = \frac{1}{T}\int_0^T z_f(t)\mathrm{d}t, \tag{1}$$

$$\widetilde{b}_{ss} = \frac{1}{\delta t_h}\int_0^T \widetilde{b}(z_{ss},t)\mathrm{d}t \tag{2}$$

$$\overline{z_{pe}} = \frac{1}{\delta t_{pe}}\int_0^T z_{pe}(t)\,\mathrm{d}t \tag{3}$$

$$\overline{z_{tr}} = \frac{1}{\delta t_{tr}}\int_0^T z_{tr}(t)\,\mathrm{d}t \tag{4}$$

where T is the acquisition time, $z_f(t)$ the instantaneous value of the fountain height, $\widetilde{b}(z_{ss},t) = b(z_{ss},t)$ when $z_f(t) \geq z_{ss}$ and $b(z_{ss},t)$ is the fountain half-width at $z = z_{ss}$. Furthermore: i) $z_{pe}(t) = z_f(t)$ when $z_f(t) \geq z_{ss} + \sigma_{ss}$, ii) $z_{tr}(t) = z_f(t)$ when $z_f(t) \leq z_{ss} - \sigma_{ss}$, and iii) δt_h, δt_{pe} and δt_{tr} are the total periods for which $z_f(t) \geq z_{ss}$, $z_f(t) \geq z_{ss} + \sigma_{ss}$ and $z_f(t) \leq z_{ss} - \sigma_{ss}$, respectively. The term σ_{ss} represents the standard deviation of the vertical fluctuation z_{ss} over the acquisition time T. In addition, we define the magnitude of the vertical fluctuations as $\delta z_{ss} = \overline{z_{pe}} - \overline{z_{tr}}$.

Figure 4 shows the comparison between the rise height statistics found in BH2012 and in the present work. The non-dimensional quasi-steady rise height, z_{ss}/r_0, and the magnitude of the vertical fluctuations, δz_{ss} (scaled both with the width of the forced fountains, $\delta z_{ss}/2\widetilde{b}_{ss}$, and with the quasi-steady rise height, $\delta z_{ss}/z_{ss}$), are well aligned. As found in BH2012, it suggests that (i) the forced fountains scale as $z_{ss} \propto r_0 Fr_0$ ($z_{ss} = 2.22\,r_0 Fr_0$ by fitting the present experiments),

Expts #	Video	ADCP	Q $(\mathrm{ml\,s^{-1}})$	r_0 (mm)	w_0 $(\mathrm{mm\,s^{-1}})$	ρ_0 $(\mathrm{kg\,m^{-3}})$	Re_0	Re_T	Fr_0
1	active	1 fixed	15.3	3.9	320	1030	1180	1059	9.5
2	active	1 fixed	15.3	3.9	320	1051	1130	894	7.3
3	active	1 fixed	15.3	3.9	320	1069	1080	817	6.2
4	active	1 fixed	15.3	3.9	320	1092	1030	755	5.4
5	active	1 fixed	15.3	3.9	320	1089	1040	762	5.5
6	no	1 moving + Cond.	15.0	3.9	314	1028	1160	1069	9.6
7	no	1 moving + Cond.	15.0	3.9	314	1021	1180	1181	11.1
8	no	2 moving	15.0	3.9	314	1060	1080	841	6.6
9	no	2 moving	15.0	3.9	314	1050	1110	888	7.2
10	no	2 moving	15.0	3.9	314	1040	1130	952	8.0
11	no	2 fixed	15.0	3.9	314	1060	1080	841	6.6
12	no	2 fixed	15.0	3.9	314	1050	1110	888	7.2
13	no	2 fixed	15.0	3.9	314	1040	1130	952	8.0
14	no	2 fixed	15.0	3.9	314	1030	1160	1045	9.3
15	no	3 moving	15.0	3.9	314	1070	1060	805	6.1
16	no	3 moving	15.0	3.9	314	1060	1080	841	6.6
17	no	3 moving	15.0	3.9	314	1050	1110	888	7.2
18	no	3 moving	15.0	3.9	314	1040	1130	952	8.0
19	no	3 moving	15.0	3.9	314	1030	1160	1045	9.3
20	no	3 moving	15.0	3.9	314	1020	1180	1201	11.4

TABLE II. Parameters of the experiments. Video indicates whether the video camera was used ("active") or not ("no"). ADCP indicates i) the number of acoustic Doppler current profilers deployed (ADCP1, ADCP2 or ADCP3), ii) if the probes were in a fixed position ("fixed") or they moved up and down ("moving"), iii) if the conductivity probe ("Cond") was present. The variables "r_0", "Q", "w_0", "Re_0", "Fr_0" and "ρ_0" are the internal radius, the source fluid discharge, velocity, Reynolds number, Froude number and density at the source section, respectively. The parameter "Re_T" represents the Reynolds number threshold at which the fountain rise height is independent of Re (see Burridge, Mistry, and Hunt[12]).

and (ii) the height of the vertical fluctuations is of the same order of the large-scale eddies at the fountains top and it is independent of Fr_0.

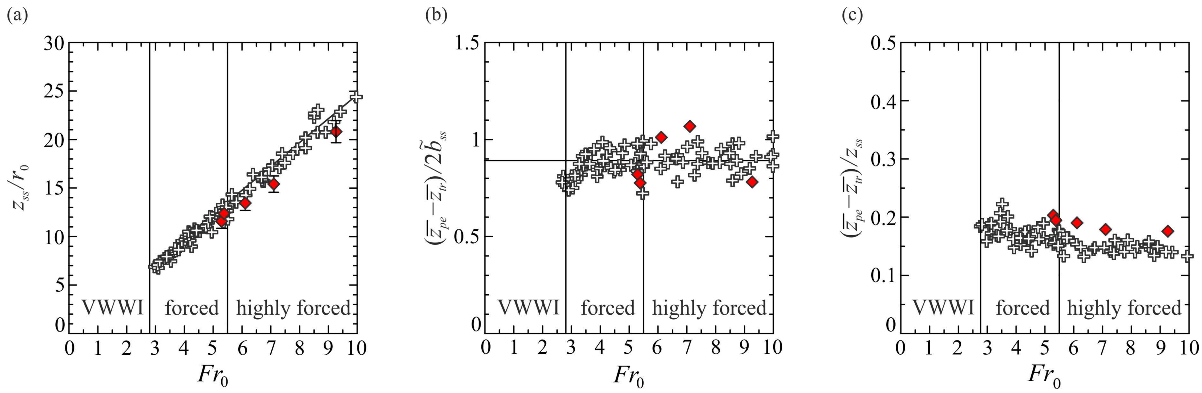

FIG. 4. Rise height statistics in the present experiments (red filled diamonds) and in BH2012 (grey filled crosses): (a) non-dimensional quasi-steady rise height z_{ss}/r_0, symbols are experimental points and solid line represents the best-fitting relation by BH2012 $z_{ss} = 2.46\, r_0\, Fr_0$ ($z_{ss} = 2.22\, r_0\, Fr_0$ considering only the present experiments); (b) vertical fluctuations scaled with the fountain width $\delta z_{ss}/2\widetilde{b}_{ss}$; and (c) vertical fluctuations scaled with the quasi-steady rise height $\delta z_{ss}/z_{ss}$). The vertical lines separate the fountains in VWWI (very weak–weak–intermediate), forced and highly-forced regimes, following the classification by BH2012.

The fluctuations of the fountain top were found in BH2013 to be prominently bi-chromatic in the frequency domain. Thus, it is possible to define a Strouhal number of the higher peak frequency, f_H, and of the lower peak frequency, f_L, as $St_H = f_H T_0$ and $St_L = f_L T_0$, respectively, where T_0 denotes an adequate time scale. A conventional time scale is represented by r_0/w_0, which results in a Strouhal number $St \propto Fr_0^{-2}$. A time scale proposed for forced fountains was w_0/g', for which the corresponding forced Strouhal number, St_{for}, appears independent of Fr_0 . Another relevant time scale comes from the large-eddies length and velocity scales, i.e. $\propto 2\widetilde{b}_{ss}/w_{ss}$, where w_{ss} is the root mean square vertical velocity of the fountain top (calculated as the time derivative of the interface signal). The latter time scale is associated with the top Strouhal number, St_{top}.

Figure 5 shows the comparison between the values of the non-dimensional found in BH2012 and in the present work. The results show a good overlap of the conventional Strouhal numbers St_H and St_L, as well as for the forced and top Strouhal numbers St_{for} and St_{top} (related to f_H).

In our experiments, we consider the quasi-steady rise height z_{ss} as the vertical length scale and the fountain width $\widetilde{b}_{ss}$ for the horizontal length scale, while the vertical and horizontal velocities

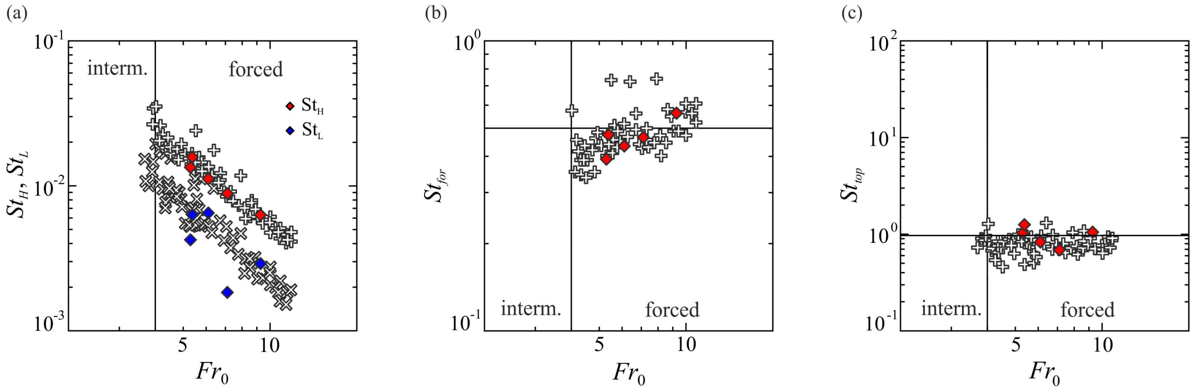

FIG. 5. Strouhal number (representing non-dimensional fluctuations peak frequencies) as a function of Fr_0. Diamonds are experiments of the present work, crosses are experiments from BH2013. (a) Conventional Strouhal number $St = fr_0/w_0$; red diamonds refer to higher peak frequency f_H, blue diamonds refer to lower peak frequency f_L; (b) Forced Strouhal number $St_{for} = f_H w_0/g'$; (c) Top Strouhal number $St_{top} = f_H 4\widetilde{b}_{ss}/w_{ss}$; the horizontal line indicate $St_{top} = 1$. The vertical line separates the fountains in intermediate and forced regimes, following the classification by BH2013.

are non-dimensional with the source flow velocity w_0.

In this study, we are not interested in the early stage of the fountain (negatively buoyant jet) which has been widely studied in recent works[23,28]. Here we want to focus on the steady state of the forced fountain, when the up- and counter-flow are both present and interact with each other.

C. Detection of the fountain interface

A well known method to extract the interface position in experimental fountains is through the use of a video camera[29], as we also did in our experiments. The image analysis we used mainly follows the same procedure reported by BH2012 and BH2013. A MATLAB script (i) extracts the pixel array above the inflow midsection at each instant, and (ii) concatenates successive arrays to built a resulting image which represents the temporal evolution of the fountain interface along z. Moreover, the sharp density interface between the salt water and the fresh water is responsible for a net discontinuity (a “jump") in the echoes number of the ADCP1 signal, which indicates the instantaneous position of the interface. Thus, we retrieved the time series of the interface fluctuations also by following the signal of the ADCP1 echoes in time (expts. 1-5). The video frames are also used to get the instantaneous vertical velocity of the interface, w_v. On the other hand, we used the ADCP1 measurements to extract the vertical velocity w_{ADCP} at z_{ss}, that is the mean rise height.

Since we have both video and ADCP measurements, we can compare the results of the two techniques in terms of temporal and spectral signals. As an example, we show the results for expts. 1 and 5, corresponding to a source flow density $\rho_0 = 1030\,\mathrm{kg\,m^{-3}}$ and $\rho_0 = 1089\,\mathrm{kg\,m^{-3}}$. Panels (a) and (b) in Figure 6 show the temporal evolution of the interface. Both the positive and the negative peaks of the signals are well-individuated by the ADCP-extracted interface, especially in the case of the lower density, which is characterized by a greater amplitude (and period) of the fluctuations. The results of the comparison of the two techniques are also reported in Table III, for both the mean value and standard deviation of the rise height. The difference between the average values is in the range $1.3-2.9$ mm, while for the standard deviation (which represents fluctuations) it is $0.2-0.6$ mm. The discrepancies are within the experimental uncertainty. Panels (c) and (d) show the time series of the velocities, w_v and w_{ADCP}. The agreement between video and ADCP data is acceptable. Some discrepancies are present and they can be explained by considering that the comparison is made between the velocity of the moving interface (video data) and the velocity measured at the mean rise height (ADCP). We also see that fluctuations of w_{ADCP} decrease with decreasing Fr_0. Finally, the spectral analysis of signals is reported in panels (e) and (f) of Figure 6. The dominant low frequency, f_L, and the dominant high frequency, f_H, of the fluctuations signal are calculated according to BH2013, and their value is compared with the power spectral density (PSD) of w_{video} and w_{ADCP}. The results qualitatively show that the dominant frequencies well represent the peak frequencies for w_v as expected, and also capture the main peaks in the spectra of the velocity w_{ADCP}.

The overall results suggest that, in order to trace the interface of two fluids with slightly different densities, the use of ADCP is comparable to the current detection methods, and it could be a good alternative to the use of a video camera. In particular, this avoids the storage of a large amount of data and the subsequent image processing.

III. RESULTS AND DISCUSSION

The present section describes the results of measurements and data processing, with the aim of characterizing the flow field in the fountain (both in axis with the jet emission and along a vertical that is 10 mm away from the same axis). The mean flow and turbulence are analysed, and for tests

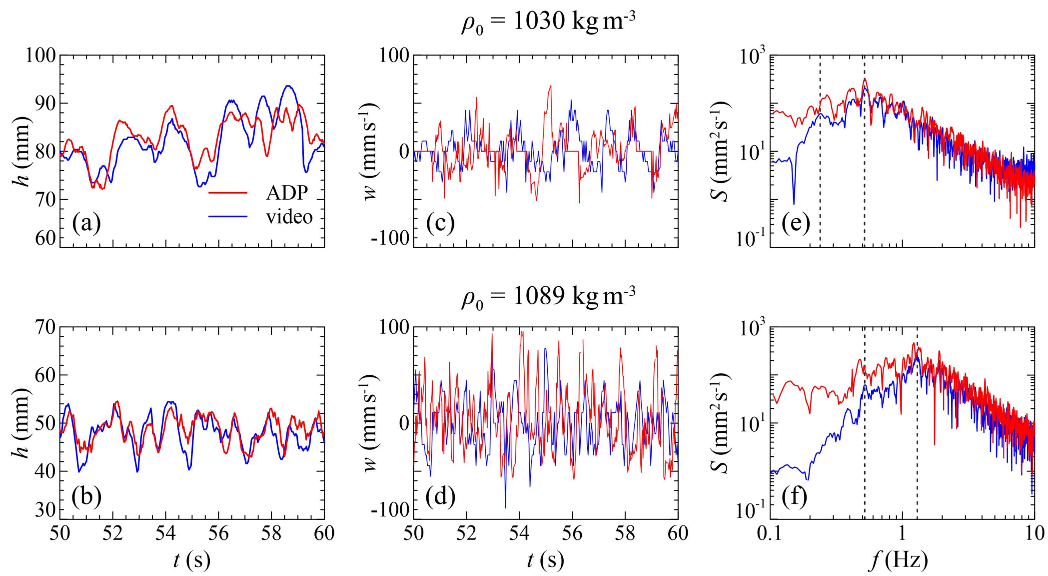

FIG. 6. Comparison of interface detection between video camera and ADCP1: panels (a) and (b) show the instantaneous interface detected by the video camera (blue lines) and extracted by the ADCP echo signal (red lines); panels (c) and (d) report the vertical velocity signal $w(t)$; panels (e) and (f) report velocity power density spectra, S (vertical dashed lines represent the lower f_L and higher f_H peak frequencies). Upper panels refer to experiment 1 ($\rho_0 = 1030\,\mathrm{kg\,m^{-3}}$), lower panels refer to experiment 6 ($\rho_0 = 1089\,\mathrm{kg\,m^{-3}}$).

6-7 also the density profile and fluctuations are taken into account.

A. The mean flow

The measured velocity is decomposed as $v(a,t) = \overline{v}(a) + v'(a,t)$, where $v(t,a)$ is the instantaneous velocity along the measuring direction a, while $\overline{v}(a)$ and $v'(t,a)$ are the mean and fluctuating components, respectively. For horizontal velocity $a = x$ and $v = u$, while for vertical velocity $a = z$ and $v = w$. The mean velocity profile is obtained by time-averaging the ADCP signal:

$$\overline{v}(a) = \frac{1}{T}\int_0^T v(t,a)\mathrm{d}t. \tag{5}$$

At each point along the vertical, the ADCP provide the measurement as an average on a circular footprint (disk) which slightly enlarges as the distance from the transducer increases. The divergence angle is $\approx 2^\circ$, which means that at the farther limit of the range (10 cm) the footprint radius is $\approx 3.5\,\mathrm{mm}$ bigger than the ultrasound source. On the opposite, the fountain widens away from the nozzle outlet (upwards). Notice that the nozzle diameter is approximately equal to the ADCP

Expt.	ρ_0	$\overline{z_{ss,v}}$	$\overline{z_{ss,D}}$	$\sigma_{z_{ss,v}}$	$\sigma_{z_{ss,D}}$
No	kg m^{-3}	mm	mm	mm	mm
1	1030	81.2	82.5	4.6	4.2
2	1051	60.1	63	3.3	2.7
3	1069	52.4	54.0	3.0	3.2
5	1089	48.4	50.0	3.0	3.4

TABLE III. Detection of the rise height of the turbulent fountain: comparison between video (subscript v) and acoustic Doppler current profilers (subscript D). Expt. indicates the number of the experiment from Table II, ρ_0 is the density at the source section, z_{ss} and $\sigma_{z_{ss}}$ are the mean and the standard deviation of the rise height, respectively.

probe transceiver, thus there must be a point in the vertical where the fountain width, $2b_u(z)$, equals the footprint diameter, $d_{ADCP}(z)$. Where $d_{ADCP}(z) > 2b_u(z)$, the measure is not reliable because it is the result of the interaction between upflow and counterflow in the footprint. This explains why we have limited the presentation of almost all the results to the lower limit of $z/z_{ss} \approx 0.4$. This only apply for ADCP1.

Figure 7(a) shows the mean vertical velocity profile of ADCP1, that is aligned to the fountain source (i.e., axial measurement). Data collapse fairly well on a single curve, with null velocity at $z/z_{ss} \approx 1.2$, and with a linear trend down to $z/z_{ss} \approx 0.4$. Beyond this limit the vertical velocities show a non monotonic profile when approaching the source inflow section; this is a non physical behaviour that can be explained if we keep in mind the operating principle of the probe (described above). The comparison between present experiments and the results by Mizushina *et al.*[15] is reported in Figure 7(b): away from the source the agreement with literature data is within the experimental uncertainty.

Figure 7(c) shows the mean vertical velocity profile of ADCP2 (non-axial measurements). Velocities are slightly negative above $z/z_{ss} \approx 1.1$, indicating the presence of the counterflow and/or of a current induced by the counterflow itself. Lower down, the behaviour is strictly related to the density of the injected fluid. For higher densities, the measurement volumes are entirely within the counterflow, with negative velocity values decreasing downward. Vice versa, in the case of lower densities, the upflow widens more and the probe registers positive velocities. Then, when the counterflow expands and invades the region next to the inlet pipe, the the measures are negative

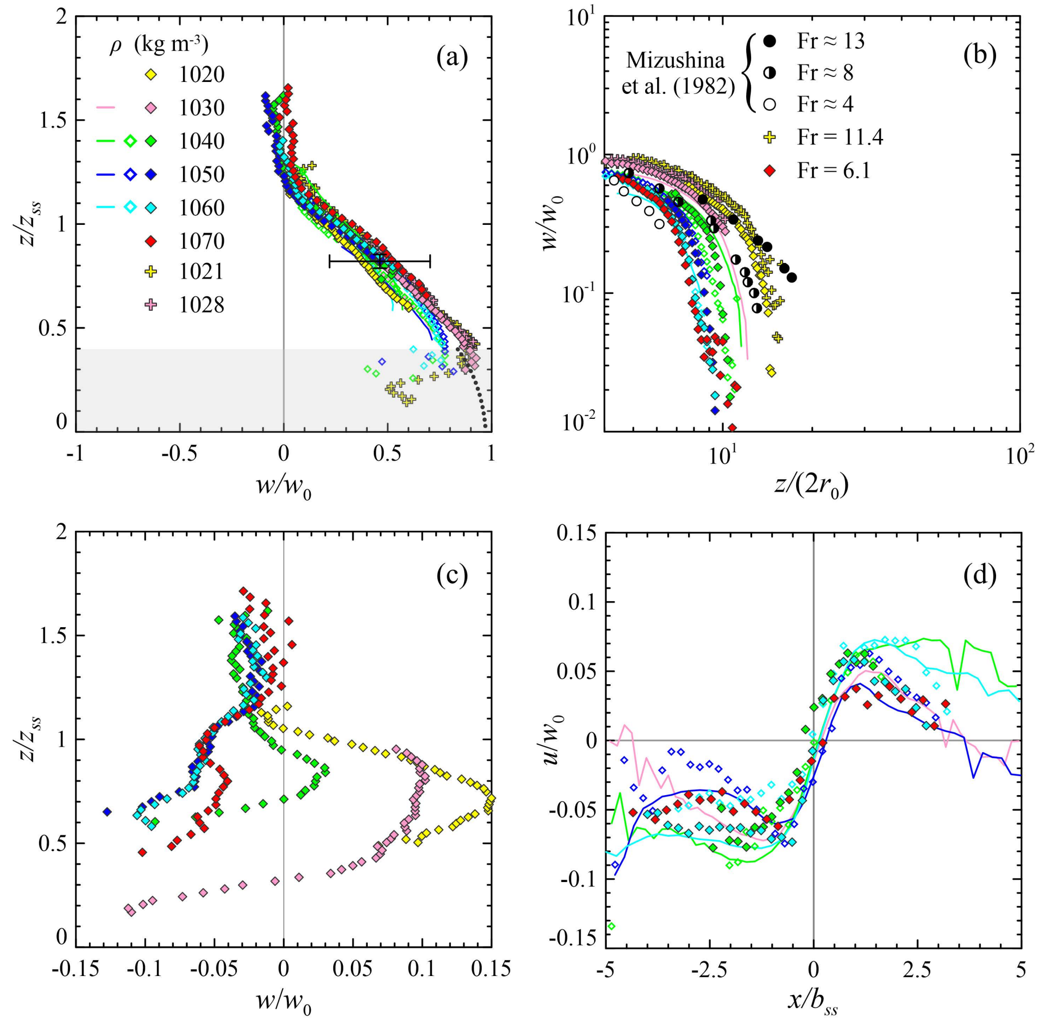

FIG. 7. Non dimensional mean velocity: (a) vertical velocity profiles for ADCP1 (axial position), the error bars refer to two standard deviations; (b) comparison between present and literature experiments; (c) vertical velocity profiles for ADCP2 (non-axial position); (d) horizontal mean velocity profiles (note that different tests have different elevations). Half-empty symbols are expts. 8-10 (2 moving ADCP), filled diamonds are expts. 16-21 (3 moving ADCP), filled crosses expts. 6-7 (1 moving ADCP plus Conduino) and solid lines are expts. 11-14 (2 fixed ADCP).

again. This offers an indirect measurements of the shape of the counterflow.

Figure 7(d) shows the mean horizontal velocity registered by ADCP3, at fixed positions. These results show how far the fountain effects are felt in terms of induced currents and recirculation. Regardless of the density of the jet, the flow field extends at least up to $x/b_{ss} \approx \pm 5$ (herein, the symbol $\tilde{}$ over b_{ss} is omitted for simplicity). Moreover, results from expts. 8-10 and 15-20, with the probes moving up and down, allow to reconstruct the horizontal velocity map. Figure 8(a) shows the results for test 16 (3 moving ADCP), which is representative for all ADCP3 data. Just above the nozzle the velocities are inward, due to the drag effect that draws ambient fluid from the surrounding areas. This favours mixing, even if the ambient fluid is only involved in the early stage of the fountain, while later it is the turn of counterflow fluid. In the upper part there is a substantial symmetry, with the flow directed towards the outside of the fountain itself. Figure 8(b) and (c) show respectively the standard deviation and the skewness of the horizontal velocity, and they will be discussed below. Notice that Figure 8 is a merge of two tests performed in the same experimental conditions, in order to cover the whole height of the fountain (Exp. 8 and 16).

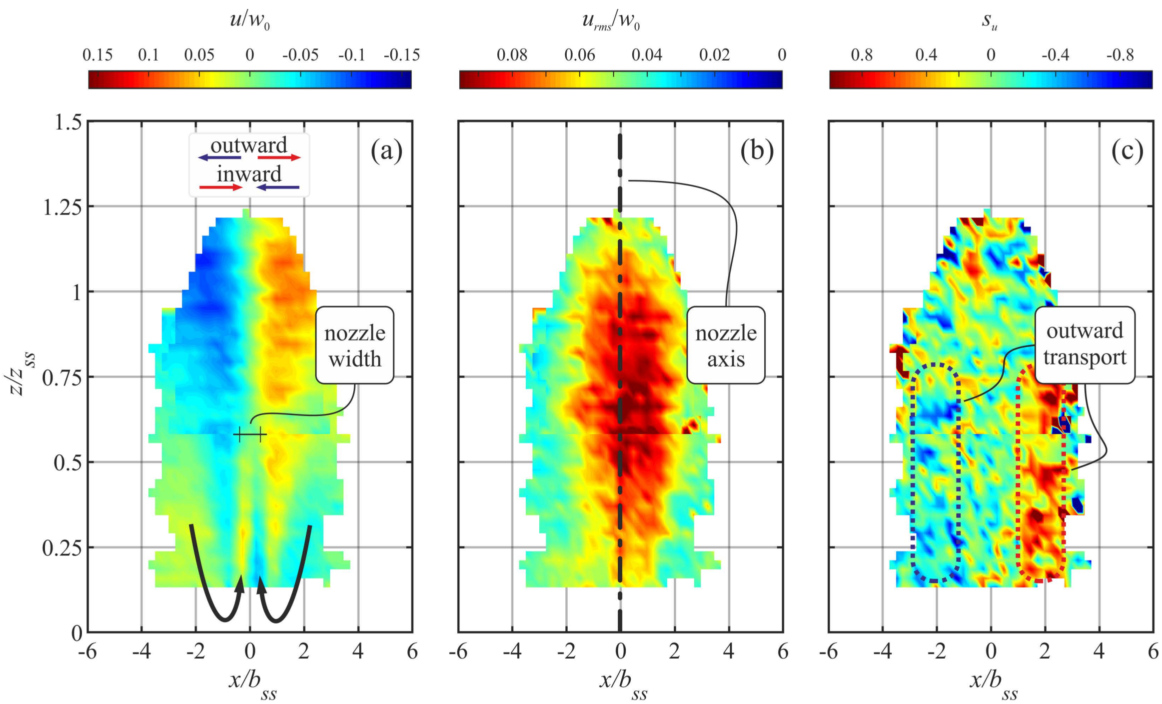

FIG. 8. Data collected by the horizontal probe (ADCP3) for tests 8 and 16: (a) horizontal average velocity map; (b) root mean square of the velocity fluctuations; (c) skewness.

B. Turbulent kinetic energy

The root mean square (RMS) of the fluctuating velocity is defined as follow:

$$v'_{rms} = \sqrt{\overline{v'^2}}, \tag{6}$$

where the overline indicates herein the time average of the argument, and the fluctuating velocity is obtained by subtracting the mean value to the whole signal, $v' = v - \overline{v}$. The quantity v'_{rms} also represents the velocity standard deviation, and it is strictly related to the two component turbulent kinetic energy TKE which is calculated as:

$$TKE = \frac{1}{2}\left(u'^2_{rms} + w'^2_{rms}\right), \tag{7}$$

Figures 9(a) and (b) report the standard deviation of the vertical velocity for ADCP1 and ADCP3. In the range $0.4 \lesssim z/z_{ss} \lesssim 1$, w'_{rms} is almost constant, with values between 0.1 and 0.16 for probe ADCP1, and between 0.8 and 0.12 for probe ADCP2. In the case of axial measurements, some tests (especially those characterized by the higher densities) present a peak at $z/z_{ss} \approx 1.1$, where the amplitude of the fluctuations is maximum. As expected, the trend of the series is then slightly decreasing upwards. In the case of ADCP3 (non-axial measurements), a density-dependent trend can be observed for $z \gtrsim 1.1$, with more intense fluctuations for higher densities. Figure 8(b) shows the map of u'_{rms}, with a magnitude of the order of w'_{rms} and higher values in the inner part of the upflow. Figure 10 shows the profile of the turbulent kinetic energy calculated with measurements

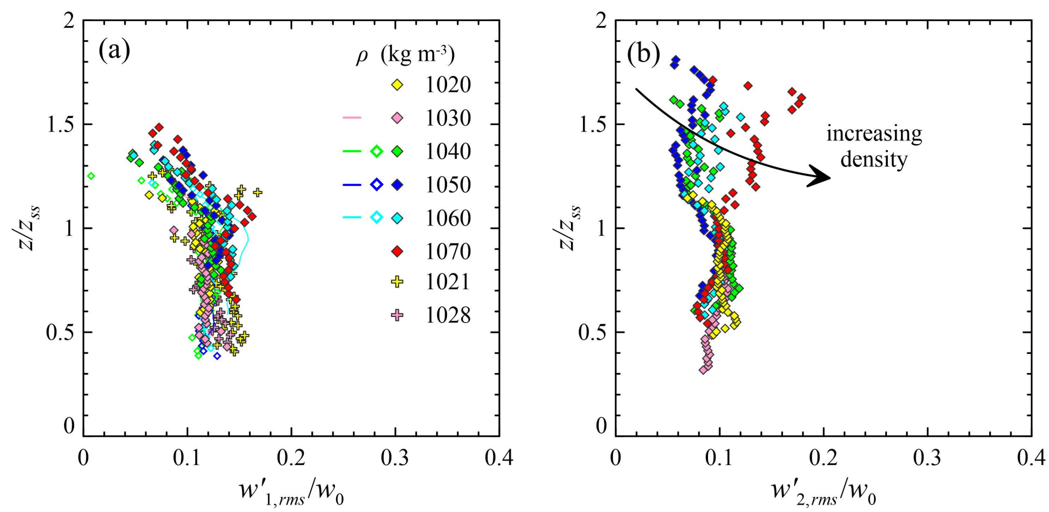

FIG. 9. Non dimensional RMS of the vertical velocity fluctuations for ADCP1 (a) and ADCP2 (b), axial and non-axial position respectively. See caption of Figure 7 for details about symbols and lines.

from ADCP1 and ADCP3. Data are slightly dispersed, but it is possible to observe a common trend with a maximum of TKE at $z/z_{ss} \approx 1$. This suggests that the turbulence is mainly developed in the upper part of the fountain (at the mean rise height), where the flow from the nozzle collides with the flow generated by the periodic collapses of the plume (rise and fall behaviour). Then, TKE decreases upwards and becomes almost null at $z/z_{ss} \approx 1.4$.

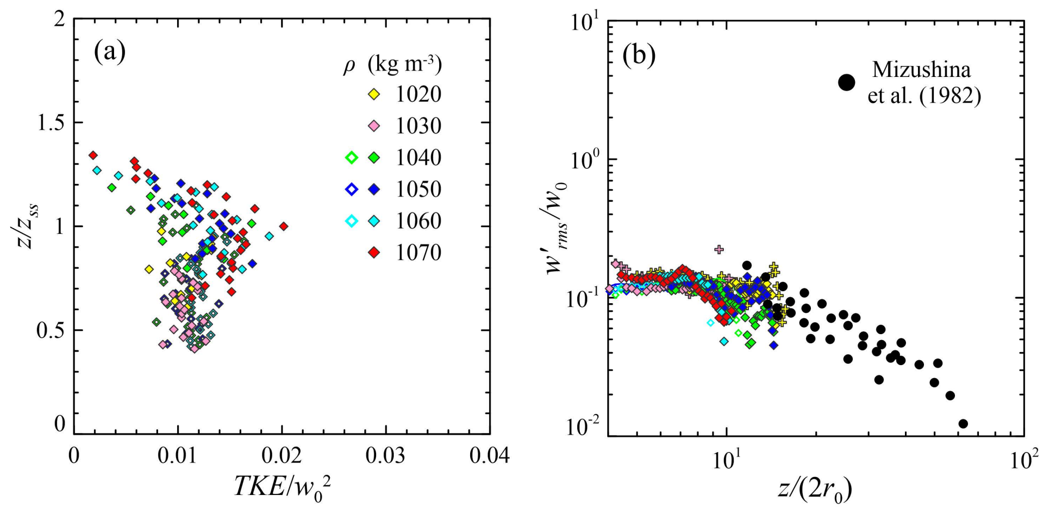

FIG. 10. (a) Two component turbulent kinetic energy (TKE) obtained using measurements from ADCP1 and ADCP3. (b) Comparison of RMS vertical fluctuating velocities w'_{rms}/w_0 at the nozzle axis between present (colored symbols) and literature experiments (black filled circles).

C. Skewness

The statistics of turbulence can also be characterized by the velocity skewness, which is an indicator of the probability density function (PDF) symmetry with respect to a Gaussian distribution. For a normal distribution, the skewness is zero. Negative values indicates that the signal distribution peak is shifted towards the right tail of the PDF, while positive values indicate that the signal distribution peak is shifted towards the left tail. The velocity skewness represents the third central moment of the velocity signal and it is calculated as

$$s_w = \frac{\overline{w'^3}}{\overline{w'^2}^{3/2}}. \tag{8}$$

for vertical velocities. The indicator s_w gives also information on the structure of the flow field[30], since the triple correlation $\overline{w'^3}$ represents the transport of $\overline{w'w'}$ by the turbulence itself. Moreover, skewness plays the same role in the equation for the evolution of turbulent kinetic energy (TKE). Hence when $\overline{w'w'}$ (and therefore skewness) is positive, both $\overline{w'w'}$ and TKE are being transported upwards. Similar considerations can be made in the case of horizontal skewness, s_u.

Figures 11(a) and (b) show the vertical skewness profiles for probe ADCP1 and ADCP2, respectively. In the case of axial measurements (ADCP1), s_w is almost null up to $z/z_{ss} \approx 1.1$. Then it decreases upward (with a minimum at $z \approx 1.4-1.5$), and finally it increases up to null or also posi-

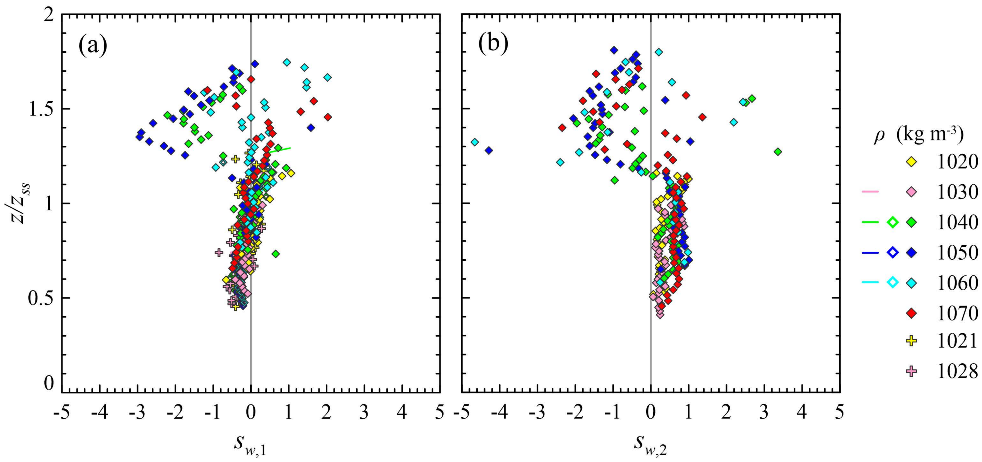

FIG. 11. Non dimensional skewness of the vertical velocity for test 16: (a) ADCP1 (axial position); (b) ADCP2 (non-axial position). See caption of Figure 7 for details about symbols and lines.

tive values (at $z/z_{ss} \approx 1.8$). We infer that in the upper part of the fountain ($z/z_{ss} > 1.1$) the transport phenomena are mainly downwards due to the formation and action of the counterflow. The experiments that exhibit positive value are those with the higher densities, for which the fluctuations seem to present an upward transport ability. In the case of non-axial measurements (ADCP2), the skewness is slightly positive in the range $0.4 < z/z_{ss} < 1.1$, which means that both $\overline{w'w'}$ and TKE are being transported upwards. For $z/z_{ss} > 1.1$, s_v is negative again (indicating transport in the downward direction).

Figure 8(c) shows the map of the horizontal velocity skewness for test 16. In the inner area of the fountain the scenario is quite varied and no particular conclusion can be drawn. On the contrary, on the sides of the the jet (in the areas enclosed in the dotted rectangles) a clear tendency to the outward transport can be observed, as a consequence of the progressive widening of the jet. Notice that the same information can be extracted from the maps referring to other tests.

D. Reynolds stresses and quadrant analysis

Substituting the mean and fluctuating components of the velocity in the momentum equation yields the turbulent stresses components, which arise from the fluctuations. For expts. 15-20, the relative position of ADCP1, ADCP2 and ADCP3 allowed us to find the overlapping measurement volume between ADCP1-ADCP3 and between ADCP2-ADCP3, and to calculate the fluctuating

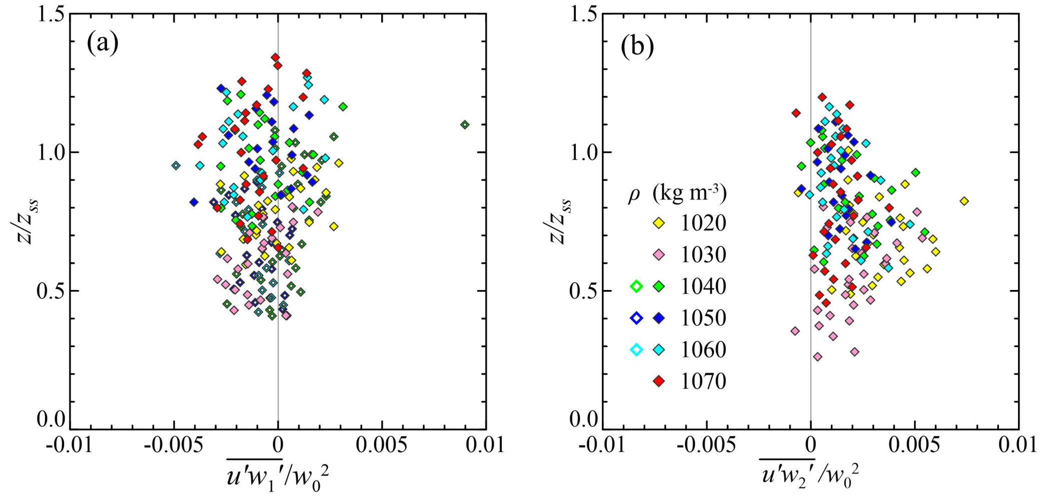

FIG. 12. Non dimensional fluctuating velocity correlations profiles: a) ADCP1-ADCP3 (axial position); b) ADCP2-ADCP3 (non-axial position). See caption of Figure 7 for details about symbols and lines.

velocity correlations $-\overline{u'w'}$, which represent the Reynolds shear stress at the net of the fluid density (note that correlation and stress have opposite sign).

Figure 12 shows the calculated non-dimensional Reynolds stresses. Even with the significant data dispersion, it is clear the different development of the axial and non-axial terms. At the nozzle axis (ADCP1-ADCP3, panel a), the shear stress profile seems to be negative on average; we also notice that the peaks are observed for higher densities and around the mean rise height, where mixing conditions are enhanced. On the contrary, the non-axial profile (ADCP1-ADCP3, panel b) is always positive and presents the largest values at $z/z_{ss} \approx 0.7$, well below the mean rise height; this is particularly true for test with lower densities, for which the plume widens not far from the nozzle.

To give a more detailed description of the turbulence structure, Reynolds shear stresses contributions are categorised according to their origin and divided into four quadrants[31]. Then, conditionally sampling according to the quadrant gives the statistics of the events, as shown in Figure 13.

The average shear stress for the i-th quadrant is

$$\overline{u'w'}_i = \frac{1}{N}\sum_{j=1}^{N}\left[u'w'\right]_i, j \text{ for i} = 1,...,4, \tag{9}$$

where N is the total number of events and j is the current sample number. The total shear stress is

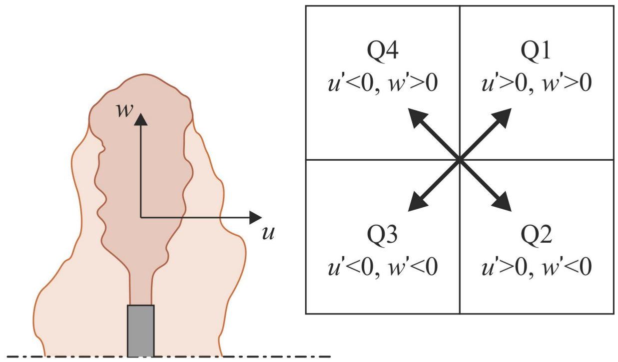

FIG. 13. Quadrant decomposition of the fluctuating components of the velocity.

$$\overline{u'w'} = \sum_{i=1}^{4} \overline{u'w'}_i. \tag{10}$$

In our experiments, we define quadrant 1 (Q1) for $u' > 0$ and $w' > 0$, quadrant 2 (Q2) for $u' < 0$ and $w' > 0$, quadrant 3 (Q3) for $u' < 0$ and $w' < 0$ and quadrant 4 (Q4) for $u' > 0$ and $w' < 0$.

Figure 14 shows the Reynolds shear stress from each quadrant using ADCP1-ADCP3 velocity correlations (in axis measurements). Q3 and Q4 show that the highest relative contributions with maximum values are reached around the rise height, indicating a out-downward transport of momentum (both to the right and to the left). On the other hand, Q1 and Q2 have similar profiles with values that are maximum near the nozzle and decrease as z/z_{ss} increases; we infer that in the region above the nozzle the transport tends to be out-upward.

The average shear stresses for ADCP1-ADCP3 velocity correlations are reported in Figure 15. In this case (and especially for low density tests), the larger shear stresses are observed in Q1 and Q3, with $\overline{u'w'}_1$ slightly larger than $\overline{u'w'}_3$ and maximum values at $z/z_{ss} = 0.7 - 0.9$. This is the area where the fountain widens and the momentum transport is mainly out-upward. The vertical profiles of $\overline{u'w'}_2$ and $\overline{u'w'}_4$ are nearly constant, but with larger values in Q4.

E. Density measurements

For expts. 6 and 7, a conductivity probe was used to measure the temporal evolution of the density vertical profile. Similarly to the velocity components, we split the density as $\rho = \overline{\rho} + \rho'$, where $\overline{\rho}$ is the mean (time-averaged) signal and ρ' is the fluctuating component obtained by subtracting the mean part to the whole signal (see §III A).

A map showing the vertical density evolution is reported in figure 16. Results suggest that the

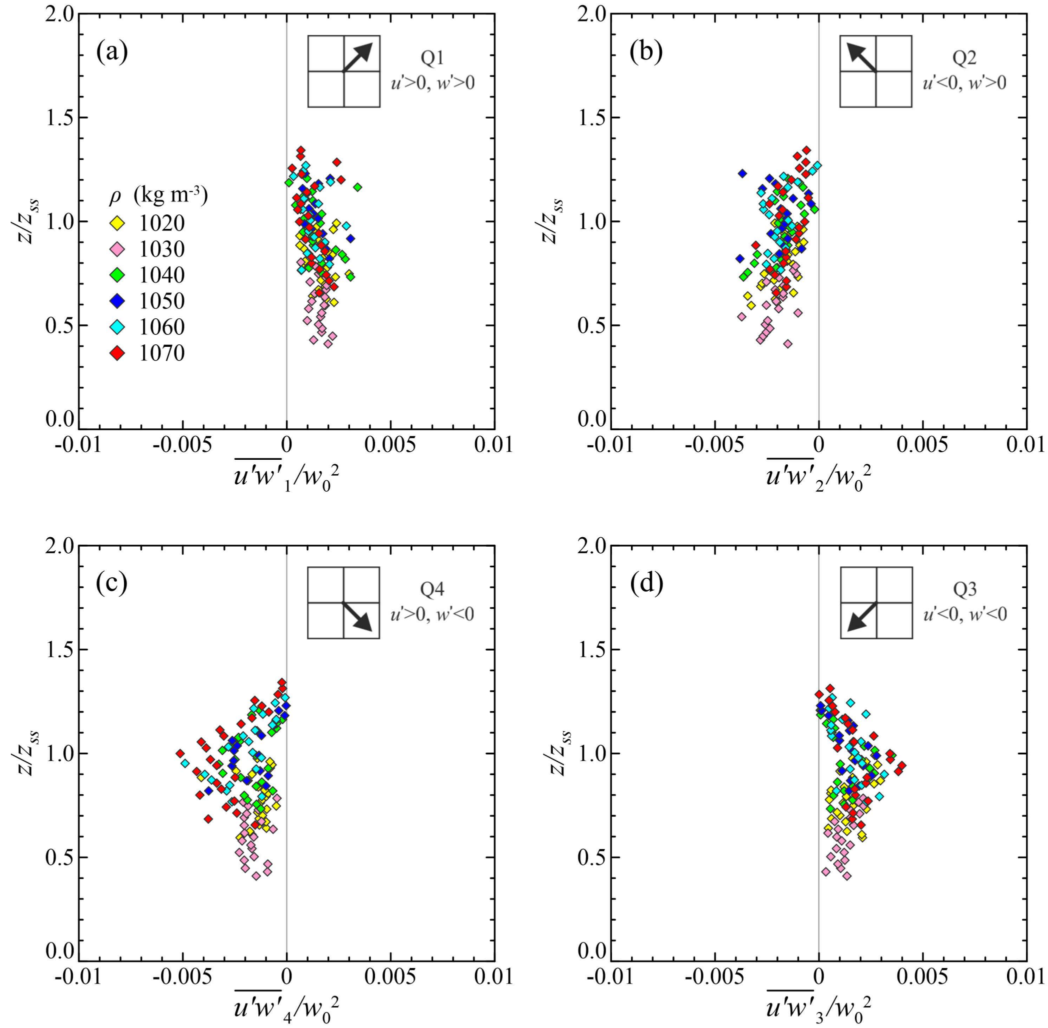

FIG. 14. Average shear stress quadrant decomposed for ADCP1-ADCP3 measurements (axial position); values are non dimensional with respect to w_0^2. See caption of Figure 7 for details about symbols.

vertical profile is subjected to fluctuations, but it is relatively stable over time (stationary) thanks to the continuous flux of source fluid which is injected and mixes with the surrounding ambient fluid.

Figure 17(a) reports the mean and fluctuating densities, $\overline{\rho}$ and ρ'_{rms} respectively. The density profile shows a maximum near the inflow and linearly decreases with the distance from the nozzle. The RMS value is nearly constant in the vertical and shows a maximum at the rise height elevation ($z/z_{ss} \approx 1$), where flow starts to reverse its direction and most of the mixing takes place. For a better comprehension of the results, we report the vertical velocity profile for both the mean and fluctuating components $\overline{w}$ and w'_{RMS}, respectively (Figure 17b). Comparing density and velocity profile, we see that the mean components have a similar trend (nearly-linear decrease with distance

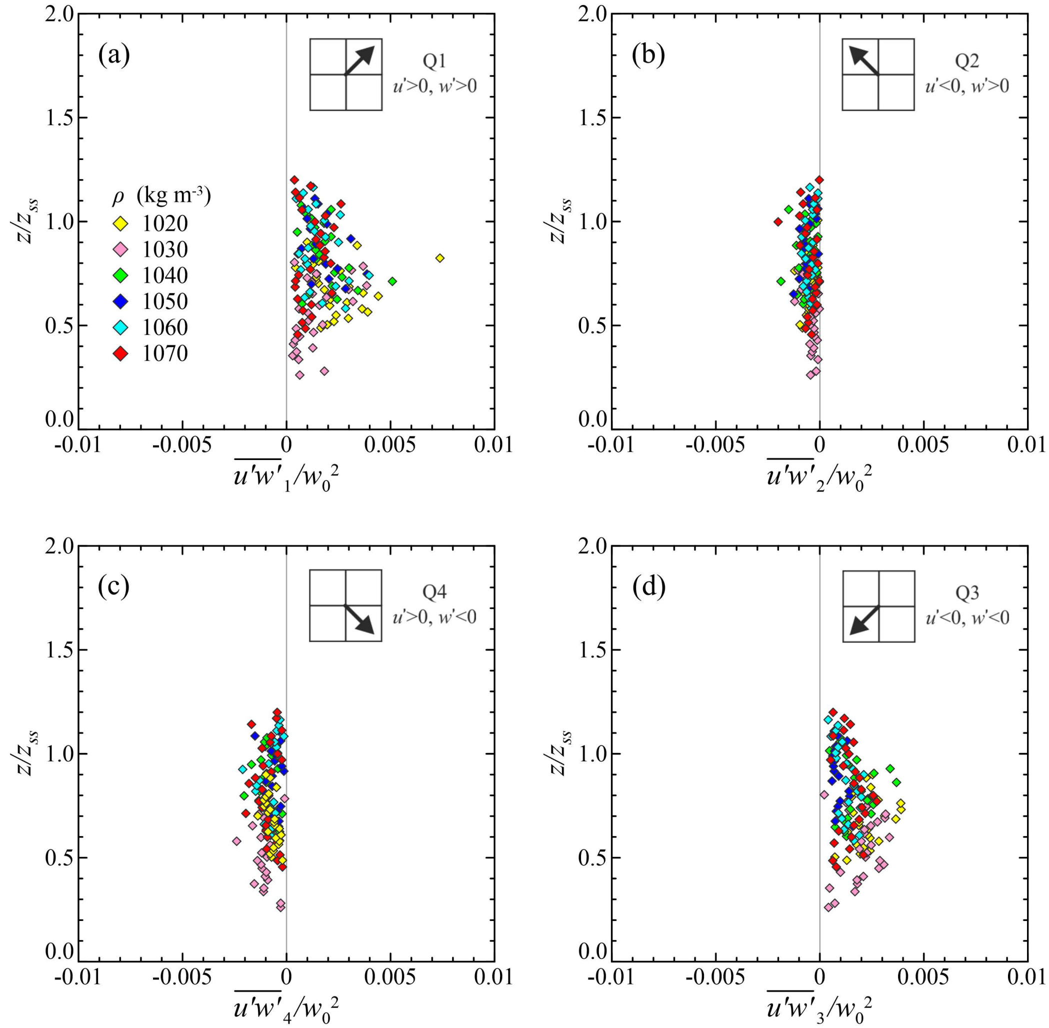

FIG. 15. Average shear stress quadrant decomposed for ADCP2-ADCP3 measurements (non-axial position); values are non dimensional with respect to w_0^2. See caption of Figure 7 for details about symbols.

from the source inflow). On the other hand the density RMS shows a maximum at the rise height, while the velocity RMS is slightly decreasing upwards (this is especially true for low density test). We also calculate the non dimensional correlation quantities $\overline{\rho}\overline{w}$ and $\rho'_{rms}w'_{rms}$ (Figure 17c), which are related to both the buoyancy and momentum fluxes, i.e. to the stabilising and acting forces of the turbulent fountains, respectively. Combining velocity, density and salinity we can retrieve crucial parameters in order to determine mixing condition, e.g. the total buoyancy flux at the midsection of the source inflow[32]. The overall results suggest that the fluctuating correlations have higher values at the mean rise height, enhancing density fluxes and mixing.

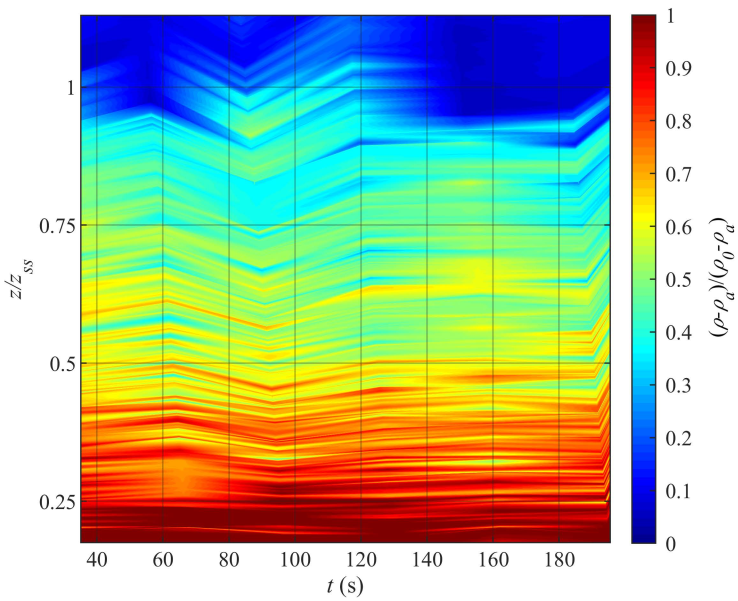

FIG. 16. Temporal evolution of the vertical density profile for expts. 6 and 7.

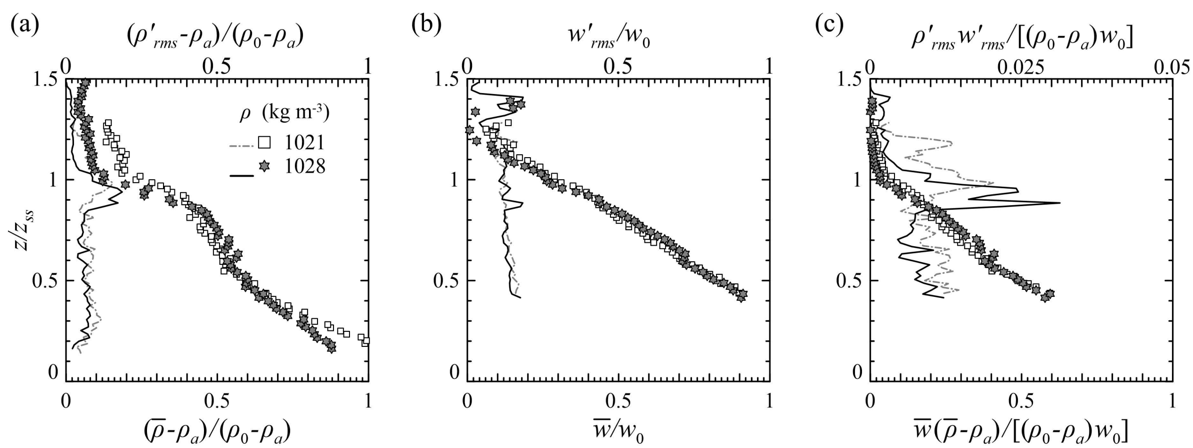

FIG. 17. (a) Vertical density profiles, (b) vertical velocities profiles, (c) profiles of correlations between density and vertical velocity. Mean values are represented with symbols and refer to the lower axes, while fluctuating values are represented by solid lines and refer to the upper axes. Results refer to expts. 6 and 7.

IV. CONCLUSIONS

The widespread occurrence of fountains, along with the scarcity of data concerning the turbulent structure of the flow field, make novel laboratory investigations a key element for further advances in the subject.

In this framework, experiments on forced fountains have been carried out in a controlled environment at the University of Parma (Italy). Present activity includes (i) measurements of the vertical and horizontal velocities in different positions, and (ii) density profiling for some of the tests. The analysis regards the mean and turbulent characteristics of the flow, and it includes details about the turbulent kinetic energy, the velocity skewness, the Reynolds stress, and the correlation between density and velocity. In order to have an idea of the variability in the radial direction, data have been collected both along axial and non-axial vertical profiles.

The acoustic Doppler current profiler (ADCP) was demonstrated to provide reliable measurements of the rise height, with the advantage of reducing the amount of data to be processed (especially when compared to image analysis techniques). On the other hand, the ADCP returns an average on a footprint whose diameter depends on the size of the probe itself, making the measurement non-punctual. This also affects the axial measurements, which we have only studied for $z/z_{ss} > 0.4$. The comparison with traditional techniques is good, both as regards fluctuations of the interface and spectral analysis.

The vertical profiles of the mean velocity collapse fairly well on a single curve (that is a straight line) for ADCP1, with null velocity at $z/z_{ss} \approx 1.2$. In the case of ADCP2, it is possible to observe the effects of the counterflow on the average velocity profiles, with a behaviour that is strictly related to the density of the injected fluid. For lower densities, the fountain has a larger horizontal spreading that is detected by the probe, thus offering an indirect measurement of the boundary between the upflow and the counterflow.

The turbulent kinetic energy shows a maximum at $z/z_{ss} \approx 1$. This suggests that the turbulence is mainly developed at the mean rise height, where the mixing between the flow from the nozzle and the flow generated by the periodic collapses of the plume takes place. Then, the turbulent kinetic energy decreases upwards and becomes almost null at $z/z_{ss} \approx 1.4$. The transport of $v'v'$ and TKE by the turbulence is mainly downward for $z/z_{ss} > 1.1$, except for tests with the higher densities. Moreover, on the sides of the jet (for $0.2 < z/z_{ss} < 0.75$) a clear tendency to the horizontal outward transport can be observed.

The Reynolds shear stress profiles are quite disperse, but a clear spatial variability can be observed: (i) at the nozzle axis, the maximum values tend to gather at the mean rise height especially for the higher densities; (ii) at non-axial position, the vertical profile is negative with peaks at $z/z_{ss} \approx 0.7$. A quadrant analysis was performed to highlight the main contributors to the stresses and their transport directions. The most relevant results are that (i) at the nozzle axis, higher shear stresses are observed in Q3 and Q4, corresponding to an out-downward transport of momentum (both to the right and to the left), with a peak at the mean rise height for higher densities; (ii) at non-axial position, the higher shear stresses are observed in Q1 and Q3, with peaks at $z/z_{ss} \approx 0.7-0.9$ for lower densities, in the area where the fountain widens and the momentum transport is mainly out-upward.

For expts. 6 and 7, the density profile presents a nearly-linear trend, decreasing with distance from the nozzle. The correlation $\rho'_{rms}v'_{rms}$, as well as the density RMS, shows a maximum at the rise height, indicating high levels of the buoyancy and momentum fluxes.

In summary, the present work aims to give a contribution for a better understanding of forced turbulent fountains, providing novel laboratory data and measurements techniques for both velocity and density.

ACKNOWLEDGEMENTS

The authors thank Prof. Sandro Longo for the stimulating discussions and the valuable suggestions, and Diana Petrolo for providing useful scripts for data analysis.

LIST OF SYMBOLS AND ABBREVIATIONS

r_0	Radial scale (internal nozzle radius)
w_0	Velocity scale (source velocity)
ρ_0	Source density
g_0'	Buoyancy
Fr_0	Source Reynolds number
Re_0	Source Reynolds number
Re_T	Threshold Reynolds number
Q	Discharge
St	Strouhal number
z_{ss}	Quasi-steady rise height
$\widetilde{b}_{ss}$	Fountain half-width
$\overline{z_{pe}}$	Mean rise height peak
$\overline{z_{tr}}$	Mean rise height trough
δz_{ss}	Magnitude of the vertical fluctuations
w	Vertical velocity
u	Horizontal velocity
s_w	Skewness of vertical velocity
s_u	Skewness of horizontal velocity
TKE	Two component Turbulent Kinetic Energy
$\overline{u'w'}$	Reynolds stress
x	Horizontal axis
z	Vertical axis
t	Time
RMS	Root Mean Square
ADCP	Acoustic Doppler Profiler
expts	Experiments

DATA AVAILABILITY

The data that support the findings of this study are available from the corresponding author upon reasonable request.

REFERENCES

[1]G. Hunt and H. Burridge, "Fountains in industry and nature," Annual Review of Fluid Mechanics **47**, 195–220 (2015).

[2]W. Baines, J. Turner, and I. Campbell, "Turbulent fountains in an open chamber," Journal of Fluid Mechanics **212**, 557–592 (1990).

[3]N. Williamson, S. Armfield, and W. Lin, "Forced turbulent fountain flow behaviour," Journal of Fluid Mechanics **671**, 535–558 (2011).

[4]Y. Lin and P. Linden, "A model for an under floor air distribution system," Energy and Buildings **37**, 399–409 (2005).

[5]G. Hunt and C. Coffey, "Characterising line fountains," Journal of Fluid Mechanics **623**, 317 (2009).

[6]J. S. Turner, "Jets and plumes with negative or reversing buoyancy," Journal of Fluid Mechanics **26**, 779–792 (1966).

[7]A. Woods and C. Caulfield, "A laboratory study of explosive volcanic eruptions," Journal of Geophysical Research: Solid Earth **97**, 6699–6712 (1992).

[8]G. Hunt and A. Debugne, "Forced fountains," J. Fluid Mech **802**, 437–463 (2016).

[9]I. Campbell and J. Turner, "Fountains in magma chambers," Journal of Petrology **30**, 885–923 (1989).

[10]N. Kaye and G. Hunt, "Weak fountains," Journal of Fluid Mechanics **558**, 319–328 (2006).

[11]H. Burridge and G. Hunt, "The rise heights of low-and high-froude-number turbulent axisymmetric fountains," Journal of Fluid Mechanics **691**, 392–416 (2012).

[12]H. Burridge, A. Mistry, and G. Hunt, "The effect of source reynolds number on the rise height of a fountain," Physics of Fluids **27**, 047101 (2015).

[13]L. Pantzlaff and R. Lueptow, "Transient positively and negatively buoyant turbulent round jets," Experiments in fluids **27**, 117–125 (1999).

[14]P. Philippe, C. Raufaste, P. Kurowski, and P. Petitjeans, "Penetration of a negatively buoyant jet in a miscible liquid," Physics of Fluids **17**, 053601 (2005).

[15]T. Mizushina, F. Ogino, H. Takeuchi, and H. Ikawa, "An experimental study of vertical turbulent jet with negative buoyancy," Wärme-und Stoffübertragung **16**, 15–21 (1982).

[16]D. Goldman and Y. Jaluria, "Effect of opposing buoyancy on the flow in free and wall jets," Journal of Fluid Mechanics **166**, 41–56 (1986).

[17]B. Morton, G. Taylor, and J. Turner, "Turbulent gravitational convection from maintained and instantaneous sources," Proceedings of the Royal Society of London. Series A. Mathematical and Physical Sciences **234**, 1–23 (1956).

[18]M. Scase and R. Hewitt, "Unsteady turbulent plume models," Journal of Fluid Mechanics **697**, 455–480 (2012).

[19]M. Woodhouse, J. Phillips, and A. Hogg, "Unsteady turbulent buoyant plumes," Journal of Fluid Mechanics **794**, 595–638 (2016).

[20]M. van Reeuwijk, J. Vassilicos, and J. Craske, "Unified description of turbulent entrainment," Journal of Fluid Mechanics **908** (2021).

[21]V. Di Federico, R. Archetti, and S. Longo, "Spreading of axisymmetric non-newtonian power-law gravity currents in porous media," Journal of Non-Newtonian Fluid Mechanics **189**, 31–39 (2012).

[22]L. Milton-McGurk, N. Williamson, S. Armfield, and M. Kirkpatrick, "Experimental investigation into turbulent negatively buoyant jets using combined piv and plif measurements," International Journal of Heat and Fluid Flow **82**, 108561 (2020).

[23]K. Talluru, S. Armfield, N. Williamson, M. Kirkpatrick, and L. Milton-McGurk, "Turbulence structure of neutral and negatively buoyant jets," Journal of Fluid Mechanics **909** (2021).

[24]C. Tropea and A. L. Yarin, *Springer handbook of experimental fluid mechanics* (Springer Science & Business Media, 2007).

[25]K. Mackenzie, "Discussion of sea water sound-speed determinations," The Journal of the Acoustical Society of America **70**, 801–806 (1981).

[26]D. Petrolo and S. Longo, "Buoyancy transfer in a two-layer system in steady state. experiments in a taylor–couette cell," Journal of Fluid Mechanics **896**, A27 (2020).

[27]H. Burridge and G. Hunt, "The rhythm of fountains: the length and time scales of rise height fluctuations at low and high froude numbers," Journal of Fluid Mechanics **728**, 91 (2013).

[28]L. Milton-McGurk, N. Williamson, S. Armfield, M. Kirkpatrick, and K. Talluru, "Entrainment and structure of negatively buoyant jets," Journal of Fluid Mechanics **911** (2021).

[29]N. Mingotti and A. Woods, "On turbulent particle fountains," Journal of Fluid Mechanics **793** (2016).

[30]M. Jiménez-Portaz, L. Chiapponi, M. Clavero, and M. Losada, "Air flow quality analysis of an open-circuit boundary layer wind tunnel and comparison with a closed-circuit wind tunnel," Physics of Fluids **32**, 125120 (2020).

[31]S. Longo and M. Losada, "Turbulent structure of air flow over wind-induced gravity waves," Experiments in fluids **53**, 369–390 (2012).

[32]D. Petrolo and A. W. Woods, "Measurements of buoyancy flux in a stratified turbulent flow," Journal of Fluid Mechanics **861** (2019).